1993ApJ...404..696V

THE ASTROPHYSICAL JOURNAL, 404:696–705, 1993 February 20

EFFECTS OF INCLINATION ANGLE ON THE SPECTRA OF X-RAY BINARIES

S. D. VRTILEK, NOAM SOKER, AND J. C. RAYMOND
Harvard-Smithsonian Center for Astrophysics, 60 Garden Street, Cambridge, MA 02138
Received 1991 June 13; accepted 1992 August 25

ABSTRACT

Iron emission and absorption features from nine X-ray binaries are compared with a model that predicts characteristics of iron K-shell features corresponding to different viewing angles for the accretion disk. In this model, emission and absorption features arise from an accretion disk corona whose structure is computed under the assumptions of ionization, thermal, and hydrostatic balance of gas illuminated by the central continuum source. Hence the equivalent widths of the emission and absorption features are predicted without the introduction of any free parameters to control the physical conditions in the disk corona. Our data/model comparison suggests an explanation for the equivalent widths of the iron Kα emission and the depth of the absorption edge in terms of (1) the angle of inclination between the observer's line of sight and the plane of the accretion disk and (2) the shape of the incident source spectrum.

Subject headings: accretion, accretion disks — X-rays: stars

1. INTRODUCTION

As the sensitivity, spectral coverage, and spectral resolution of satellite-borne instruments for X-ray astronomy have increased, so have the number and complexity of models proposed to fit the *continuum* spectra for binary systems. Unfortunately, none of the proposed continuum models is unique, no single model provides adequate fits to all the observations of even a single source, and, disturbingly, analyses based on different instruments appear to favor different models (Ponman, Foster, & Ross 1990, hereafter PFR90; Vacca et al. 1987; Vrtilek et al. 1986). This lack of uniqueness in continuum models that give satisfactory fits to X-ray spectra makes physical interpretations of the model parameters difficult. Vrtilek, Swank, & Kallman (1988, hereafter VSK88) have shown that the difficulties in finding unique and physically meaningful models for X-ray continuum spectra are exacerbated by the presence of strong, variable emission and absorption features that are not resolved by most of the instruments observing them. There is no doubt that the addition of line features leads to dramatic improvement in the quality of continuum spectra fits (Chiappetti et al. 1990; Kallman, Vrtilek, & Kahn 1989; Makishima 1986, hereafter M86; White et al. 1986, hereafter W86; Brinkman et al. 1985). Unfortunately, very few instruments have had sufficient energy resolution and throughput to detect most X-ray line features.

The iron K-shell features between 6 and 7 keV are the exception because their location in energy places them at the center of the range most observed by X-ray instruments; they are the *only* sharp spectral features strong enough to be detected by the majority of the instruments flown to date. Since iron is the most abundant heavy element in the universe, has a high fluorescent yield, and appears to be common in the spectra of many celestial objects, iron is a useful and widely observed "tracer" of the matter distribution within both Galactic and extragalactic X-ray sources. The depth and energy of the iron K-edge feature and the equivalent width and energy of the iron Kα line provide good diagnostics of the geometric structure and elemental composition of the material surrounding X-ray binary systems (M86; Inoue 1985, hereafter I85; Nagase et al. 1986, hereafter N86).

We compare observations of the iron K-shell features from a selection of X-ray binaries with a recently developed model which calculates the radiative transfer through an acretion disk corona (ADC). ADC models have generally been derived from theoretical considerations of X-ray heating and hydrostatic equilibrium (Fabian, Guilbert, & Ross 1982, hereafter FGR82; Begelman, McKee, & Shields 1983, hereafter BMS83) or from light-curve models based on bulges at the edge of the disk (White & Holt 1982, hereafter WH82). We have extended the theoretical models by including a more complete treatment of heating and cooling in the X-ray–illuminated gas and by making two-dimensional Monte Carlo calculations for the radiative transfer. The model provides good fits to the observed iron K-shell features of many X-ray binaries, with differences in the shape and intensity of the features attributed to the angle of inclination of the source to the observer and to the shape of the incident spectrum.

In § 2 we give brief descriptions of the observations and observing instruments, in § 3 we describe the model, in § 4 we present the results from a comparison of the data and models, and in § 5 we discuss the implication of these results for our current understanding of X-ray binaries.

2. OBSERVATIONS

Recent instrumental improvements and theoretical advances have combined to allow use of the X-ray spectral features of iron as diagnostic tools. The factor of 2 improvement in energy resolution of the Gas Scintillation Proportional Counters (GSPCs) on *Tenma* and *EXOSAT* over conventional proportional counters has allowed detection of the iron K-shell features in almost every class of X-ray source. The GSPCs on *Tenma*, described in detail by Koyama et al. (1984), cover the energy range 2–35 keV; their peak effective area, 640 cm^2, is at 6 keV, where the energy resolution is 9%. The GSPC on *EXOSAT* is described in detail by Peacock et al. (1982); the detector has a spectral resolution of 10% at 6 keV and a peak effective area of 160 cm^2. The *EXOSAT* GSPC could be operated in two gain modes which gave energy ranges of 2–16 keV or 2–24 keV.

We have compiled observations of all X-ray binaries

TABLE 1

LOG OF SOURCES[a]

Source	Binary Period[b] (days)	Pulse Period[b] (s)	R_m[c] (cm)	Inclination Angle (deg)	Energy of Fe Line[d] (keV)	Equivalent Width of Fe Line[d] (eV)	Energy of Fe K-Edge[d] (keV)	References[e]
High-Mass X-Ray Binaries								
4U 0115−73 (SMC X-1)	3.89	0.7	1.3×10^8	65^{+12}_{-9}[f]	6.1	113	No edge	DB
4U 1119−60 (Cen X-3)	2.09	4.8	1.1×10^8	≥ 63[g]	6.6 (6.4–6.6)	188 (100–200)	No edge (no edge)	DB (I85, Koy85)
4U 1956+35 (Cyg X-1)	5.60	...	...	36–67[h]	6.0–6.4 (6.4–6.6)	90–140 (20–84)	No edge (no edge; 7.2)	BWP85 (Kel90; M86)
Low-Mass X-Ray Binaries								
4U 1254−69	0.16[i]	...	...	65–80[i]	6.5	45–80	No edge	C86
4U 1617−15 (Sco X-1)	0.79	...	...	25–30[j]	6.7 (6.7)	20–50 (8–40)	No edge (no edge)	WPT85 (H87)
4U 1656+35 (Her X-1)	1.7	1.24	1.1×10^8	80^{+8}_{-5}[f]	6.4–6.7 (6.7)	50–200 (100–200)	8.3 (7.2)	K85, K87 (M86)
4U 1735−44	0.19[k]	...	...	10–20[l]	6.6	60–120	No edge	PFR90
4U 1822−37	0.23	...	...	70–80[m]	6.6	161	No edge	DB
4U 2142+38 (Cyg X-2)	9.84	...	...	65–75[n]	6.6–6.9 (6.7)	20–60 (30)	No edge	H86 (H87)

[a] All values listed in Table 1 are taken from the literature.

[b] Binary and pulse periods are from Bradt & McClintock 1983 unless otherwise noted.

[c] Magnetospheric radius given by 1.5×10^8 (cm) $P^{2/3}(M_{ns}/M_{\odot})^{1/3}$, where P is the pulse period in seconds.

[d] Values taken from observations with the GSPC on *EXOSAT*; when available, values in parentheses refer to observations taken with the GSPC on *Tenma*.

[e] References apply to Fe line and edge data; DB refers to values taken from the display pages of the *EXOSAT* data base. References not cited in text! C86: Courvoisier et al. 1986; H86: Hasinger et al. 1986; H87; Hirano et al. 1987; K85: Kahabka et al. 1985; K87: Kahabka 1987; Kel90: Kitamoto et al. 1990; WPT85: White, Peacock, & Taylor 1985.

[f] Nagase 1989.

[g] Clark, Minato, & Mi 1988.

[h] Davis & Hartman 1983.

[i] Motch et al. 1987.

[j] Crampton et al. 1976.

[k] Corbet et al. 1986.

[l] Smale & Corbet 1991.

[m] Cowley, Crampton, & Hutchings 1982.

[n] Cowley, Crampton, & Hutchings 1979.

thought to be predominantly disk-fed, and with known inclinations, that were detected by the *EXOSAT* GSPC with sufficient statistics to determine the strengths of spectral features. These comprise three high-mass X-ray binaries (HMXBs) and six low-mass X-ray binaries (LMXBs), of which three are pulsing and six are nonpulsing systems. We do not include long-period pulsing systems, since the neutron star magnetic field may disrupt the disk at large radii (see § 3.2). Table 1 lists some characteristics of the sources, including the inclination angle of the source and, where available, previously reported values of the strength and position of the iron line and edge as detected by *EXOSAT* and *Tenma*. In several cases, the reported equivalent widths for a given source are very different in the two instruments; we suggest that some of this variation can be attributed to the fact that an iron edge has not been included in the fits to the *EXOSAT* data. We have therefore reanalyzed the *EXOSAT* archival spectra of all the sources.

Table 2 lists the parameters obtained from the best-fit models as found for the data we extracted from the *EXOSAT* archives. Sample spectra of the analyzed sources, arranged in order of increasing inclination angle, are shown in Figure 1 along with the best-fit model with the parameters listed in Table 2. The feature near 4.8 keV is an instrumental effect due to the L-edge of the xenon detector gas that is not properly dealt with by the response matrices provided by *EXOSAT* (F. Haberl & T. Belloni 1992, private communication). Thus we exclude the region between 4.2 and 5.3 keV. In addition, the *EXOSAT* GSPC has difficulty determining the neutral hydrogen column density to the source. Where possible, we constrain the column density to values we derived from simultaneous low-energy observations taken with the *EXOSAT* low-energy detector. Since we are primarily interested in measuring the spectral features, any good fit to the continuum data suffices: we used simple power laws, with only one adjustable parameter, to fit the continuum (excluding the regions where spectral features are expected). Since power laws proved inadequate over the full energy range for the brighter sources, we restricted the range of the fit to the region between 3.0 and 10 keV. Once we have determined a power-law index, we then fit the range from 3.0 to 20 keV (or 3.0 to 10 keV for the strong sources), in order to determine the parameters of the line and edge features.

3. ACCRETION DISK CORONA MODEL

Evidence for the presence of accretion disk coronae in X-ray binaries is found in extended X-ray eclipses independent of energy that have been observed in several LMXBs (WH82; McClintock et al. 1982; Mason 1986). Theoretical studies of the effects of heating by a central X-ray source on the structure of accretion disks also predict substantial amounts of material above the disk plane that has been "evaporated" from the disk surface (FGR82; BMS83).

We assume that an X-ray binary system can be viewed as a point source of X-rays propagating through the ADC. We have developed and tested such an ADC model using simulta-

TABLE 2

SPECTRAL PARAMETERS[a]

Source	Date of Observation (yr.day)	Binary[b] Phase Range	N_{PL}[c] ($cm^{-2}\,s^{-1}\,keV^{-1}$)	α	log N_H (cm^{-2})	Fe-Line Energy (keV)	Fe Line EW (eV)	Fe K-Edge Energy (keV)	χ^2/dof
				High-Mass X-Ray Binaries					
4U 0115−73..........	84.303	0.47–0.52[d]	1.4 ± 0.6	1.4 ± 0.1	22.2 ± 0.2	6.1 ± 0.2	90 ± 18	No edge	117/107
4U 1119−60..........	85.066	0.54–0.78[e]	21.6 ± 2.0	1.3 ± 0.1	22.6 ± 0.2	6.6 ± 0.2	85 ± 15	No edge	57/39
4U 1956+35..........	85.224	0.26–0.30[f]	21.9 ± 2.0	1.5 ± 0.1	19.6 ± 0.1	6.5 ± 0.1	71 ± 14	7.5 ± 0.2	130/101
				Low-Mass X-Ray Binaries					
4U 1254−69..........	84.036	0.26–0.75[g]	13.2 ± 0.5	2.6 ± 0.1	22.5 ± 0.2	6.0 ± 0.1	36 ± 6	9.5 ± 0.2	92/80
4U 1617−15..........	84.071	0.68–0.75[h]	3981.0 ± 400.0	2.4 ± 0.3	22.6 ± 0.2	6.8 ± 0.3	44 ± 9	No edge	120/36
4U 1656+35..........	84.076	0.43–0.59[i,j]	1.9 ± 0.4	1.1 ± 0.1	22.6 ± 0.2	6.6 ± 0.1	145 ± 29	7.4 ± 0.2	125/115
4U 1656+35..........	84.061	0.65–0.69[i,k]	3.1 ± 1.0	1.0 ± 0.1	21.8 ± 0.2	6.5 ± 0.1	156 ± 30	7.4 ± 0.2	131/112
4U 1735−44..........	85.230	0.22–0.72[l]	37.2 ± 2.0	2.2 ± 0.1	22.3 ± 0.2	7.1 ± 0.2	47 ± 8	No edge	50/32
4U 1822−37..........	84.263	0.25–0.75[m]	3.1 ± 1.0	1.5 ± 0.1	22.7 ± 0.1	6.7 ± 0.2	71 ± 14	9.3 ± 0.2	103/74
4U 2142+38..........	83.261	0.33–0.35[n]	110.0 ± 10.0	2.9 ± 0.2	22.6 ± 0.2	7.0 ± 0.2	30 ± 8	No edge	175/98

[a] All values listed in Table 2 were determined by the authors using *EXOSAT* GSPC archive data.

[b] Binary phase range, where phase 0.0 refers to X-ray eclipse.

[c] Assumed photon flux has the form

$$N(E)(\mathrm{cm}^{-2}\ \mathrm{s}^{-1}\ \mathrm{keV}^{-1}) = [N_{\mathrm{PL}}(E)^{-\alpha} + N_{\mathrm{line}}\,\delta(E - E_{\mathrm{line}})](e^{-N_{\mathrm{H}}\sigma(E)})(e^{-N_{\mathrm{Fe}}\sigma_{\mathrm{Fe}}(E)})\ ,$$

where E is in keV, $\sigma(E)$ is the photoelectric absorption cross section obtained by considering the effect of all the heavy elements at their cosmic abundances as given by Morrison & McCammon 1983, N_H is the total hydrogen column density, $\sigma_{Fe}(E)$ is the photoelectric absorption cross section of Fe (assumed zero if $E < E_{edge}$ and $9.54(E_{edge}/E)^{2.84}$ if $E > E_{edge}$), and N_{Fe} is the column density of absorbing iron atoms. The Fe-line feature, unresolved by *EXOSAT* and *Tenma*, is modeled as a delta function of adjustable energy-integrated flux.

[d] Bonnet-Bidaud & van der Klis 1981: T_0 = JD 2,443,116.9446 and P_{orb} = 3.89239 days.

[e] Kelly et al. 1983: T_0 = JD 2,440,958.8509 and P_{orb} = 2.087139 days.

[f] Bolton 1975: T_0 = JD 2,441,556.46 and P_{orb} = 5.599824 days.

[g] Motch et al. 1987: T_0 = JD 2,445,735.693 and P_{orb} = 0.163890 days.

[h] Crampton et al. 1976: T_0 = JD 2,442,565.741 and P_{orb} = 0.787313 days.

[i] Deeter, Boynton, & Pravdo 1981: T_0 = JD 2,441,329.57519 and P_{orb} = 1.70016773 days.

[j] Phase 0.67 of 35 day cycle: low-on state.

[k] Phase 0.23 of 35 day cycle: high-on state.

[l] Corbet et al. 1986: T_0 = HJD 2,446,290.351 and P_{orb} = 4.654 hr.

[m] Hellier et al. 1990: T_0 = JD 2,445,615.30961 and P_{orb} = 0.232108782 days.

[n] Cowley, Crampton, & Hutchings 1979: T_0 = JD 2,443,161.68 and P_{orb} = 9.843 days.

1993ApJ...404..696V

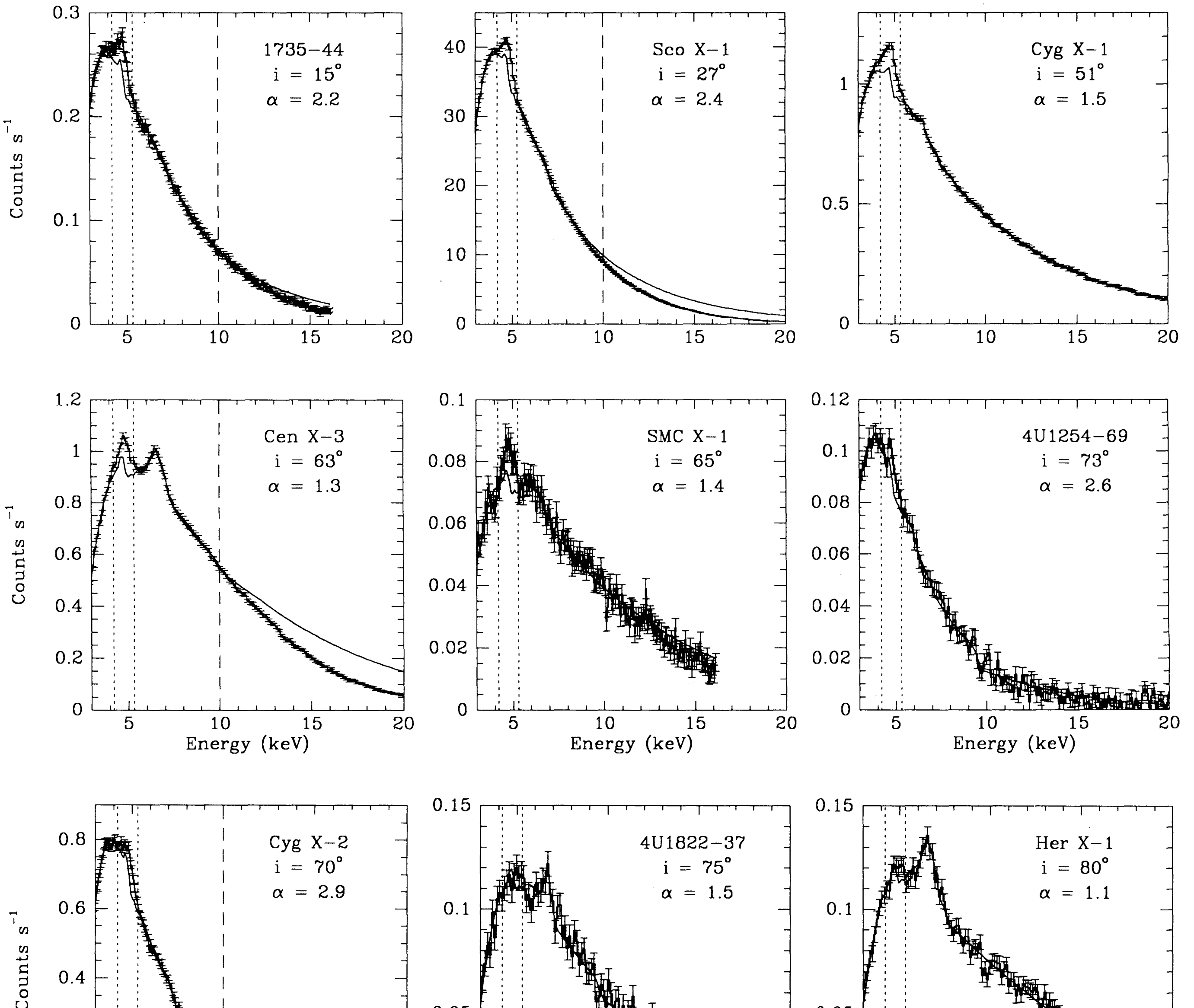

FIG. 1.—Sample *EXOSAT* GSPC spectra of the objects listed in Table 1 arranged in order of increasing inclination angle. The solid line represents the best-fit model with the parameter values noted in Table 2. Dashed lines at 10 keV indicate those bright sources for which the spectra were fitted in the 3–10 keV range only. Short-dashed lines at 4.3 and 5.2 keV indicate region excluded from fit because of improper response function.

neous X-ray, optical, and UV observations of two objects, Cyg X-2 and Sco X-1: taking the observed X-ray luminosities, we could reproduce the observed optical and UV continua and line fluxes through X-ray heating of an ADC (Vrtilek et al. 1990, 1991; Kallman, Raymond, & Vrtilek 1991). Cyg X-2 and Sco X-1 are so-called "Z-sources," sources which show three distinct patterns of temporal and spectral behavior. Our previous work was able to identify the changes between these three states with changes in the mass transfer rate: since the continuum shape and the derived outer disk radius for a given source did not vary with spectral state, the disk structure can be considered invariant with X-ray spectral state (Vrtilek et al. 1990, 1991). The outer disk radius we have assumed here (10^{11} cm) is intermediate between those required for Cyg X-2 (6×10^{11} cm) and Sco X-1 (6×10^{10} cm). As the larger disk radii contribute mostly to the optical emission, the size we adopt here should not affect the X-ray emission. A very large disk may make the inclination at which the equivalent width of Fe increases a little farther from 90°.

This paper is the *first* attempt to apply this model to our understanding of the iron K-shell features that are ubiquitous in X-ray binaries. Although the line *flux* in the UV, optical, and X-ray regions was shown to increase with increase in mass accretion rate, the line *equivalent widths* remain constant (Vrtilek et al. 1991; Hasinger et al. 1990). Hence, we use observed line equivalent widths, which should be independent of source state, to compare with our model predictions. We make no attempt to address modulation due to orbital motion: rather we use observations taken during binary phases 0.25–0.75 (where 0.0 is the X-ray eclipse) to ensure that we are looking directly at the X-ray source. Radiative transfer through the ADC is calculated using a Monte Carlo code described in § 3.2.

3.1. *Disk Corona Structure*

The density structure of the ADC is computed in two stages. First the photospheric temperature of the disk is calculated as a function of radius; then a series of one-dimensional vertical models is computed.

The disk temperature as a function of radius is computed from the local viscous dissipation (which depends on $\dot{M}$), the assumed neutron star mass (1.4 $M_{\odot}$), and heating by X-ray illumination. For these models we assume direct, unattenuated illumination from the central source. The effects of attenuation will be considered in a subsequent paper; preliminary results show that the current model does not differ much from the self-consistent models (Soker & Raymond 1993). The heating rate depends on the local slope of the disk surface, but because this depends in turn on the temperature, iteration is required. We assume an albedo of 0.5 (Basko, Sunyaev, & Titarchuk 1974). X-ray heating dominates in the outer part of the disk, while local viscous dissipation dominates within about 10^{10} cm.

The one-dimensional (i.e., radius-dependent) models begin with the disk temperature, the mass accretion rate, $\dot{M}$, and a viscosity parameter. These determine the vertical density structure of the disk below the photosphere. For a given X-ray illumination, an initial guess at a hydrostatic corona is matched to this disk by balancing Compton heating and cooling against bremsstrahlung cooling (see FGR82). The vertical structure code then takes the initial guess or the model from the previous iteration and computes the ionization balance, the photoabsorption heating, and the emission-line cooling of the dozen most abundant elements. A temperature structure is determined from the energy balance, and that temperature structure is used to compute a new hydrostatic density structure. Iteration produces self-consistent vertical temperature and density profiles. The results resemble those of FGR82 fairly closely in the innermost parts of the disk, but a lower coronal zone at a temperature around $10^{6.2}$ K (where photoionization heating balances recombination cooling, with iron the dominant contributor to both) covers most of the disk. The temperature of this zone determines the pressure and density in the Compton-heated layers above it, and the partially ionized iron in the lower coronal zone contributes significantly to the Kα emission. The density contour map of the disk in the radial distance–angle plane is given in Figure 2. Above the outer regions of the disk, the ADC forms a thermally driven wind instead of a hydrostatic structure (BMS83; Ostriker, McKee, & Klien 1990). The density structure will certainly be affected, but the flow should be subsonic in the relatively high-density regions where the iron emission and absorption occur. A nonhydrostatic ADC may have a density inversion (Melia, Zylstra, & Fryxell 1991) which could alter the inclination dependence of equivalent width: high equivalent widths might occur at somewhat lower inclination angles.

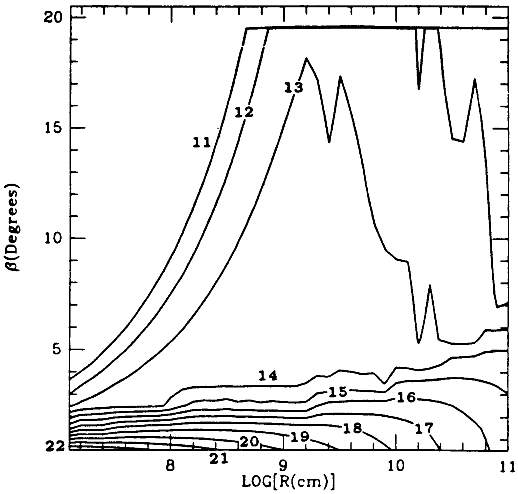

FIG. 2.—Electron density contours of the disk corona in the (R, β)-plane, where R is the radial distance from the neutron star and β is the angle from the equatorial plane. The corona is truncated at $\beta = 20°$. The contour levels are equally spaced on a logarithmic scale from 10^{11} to 10^{22} cm^{-3}.

3.2. *Two-dimensional Monte Carlo Computational Approach*

The Monte Carlo scheme for Compton scattering is based upon the work of Pozdnyakov, Sobol, & Syunyaev (1983, hereafter PSS83). Since we are dealing only with cool gas, we use the approximation of low temperature to calculate the mean free path for electron scattering. The radiation is represented by a large number of particles which move inside a three-dimensional grid. The particles, which represent photons, are injected at the origin. The temperature, density, and ionization level of iron in the accretion disk are given in each cell by the 10 ADC models described above. At each step a mean free path is calculated for each particle according to the physical conditions in the cell it resides in. From this, a random distance is picked as described in PSS83, with the addition that here we have absorption and scattering by iron ions. The total abundance of iron atoms relative to hydrogen atoms is 3×10^{-5} (appropriate for cosmic abundances taken from Morrison & McCammon 1983). Once the L-shell is filled, the Kα energy remains fairly constant. Thus we lump all the low-ionization stages together as Fe XVIII. This precludes a detailed prediction of the line profile or energy centroid; here we concentrate on equivalent width. In the inner disk, the ADC model predicts a low-ionization disk, a thin ($\leq 0\overset{\circ}{.}1$) zone of intermediate ionization, and the highly ionized species Fe XXV, Fe XXVI, and Fe XXVII above. In the outer disk, beyond about 10^{10} cm, the structure is similar except that the intermediate-ionization zone is around 1° in thickness.

The particles are not allowed to move more than a distance $D_{\max}$, taken to be 50% of the cell size (in the direction of propagation), in a single step. If the distance is less than $D_{\max}$, the particle is being absorbed by an iron ion or scattered by an electron, according to the probability of each process. Each particle is characterized by an energy and by a weight which is proportional to the number of photons the particle represents. The particles are injected with random energies in the interval

4–20 keV; the probabilities are adjusted as a function of energy to result in a power-law spectrum.

$$N_\gamma(E) \propto E^{-\alpha}\,, \tag{1}$$

where N_γ is the number of photons. Each particle starts its trajectory at the neutron star, which is at the center of the grid, with a random direction (isotropic radiation).

Particles which leave the grid or which are well inside the optically thick regions of the disk—George & Fabian (1991) have shown that the removal from the simulations of particles which are inside an optical depth of 5 is justified—are removed from the simulation and their properties are recorded. The K-edge energies are as in M86, and cross sections for processes concerning iron are as in George & Fabian (1991). The yield for the different ions, i.e., the probability that an absorption will end with emission of a K line, are taken from Mertz, Cowan, & Magee (1976). Each particle which is absorbed, by either bound-free or bound-bound processes, is reemitted in a random direction with the energy of the appropriate line and its weight is the yield for this process times its weight before the absorption.

The boundaries of the grid cells are

$$1^\circ(i-1) < \beta \leq 1^\circ i \quad \text{for} \quad i = 1, 2, \ldots, 20$$

and

$$0.1(j-1) < \log\,(r/10^{7.05}\ \text{cm} \leq 0.1j \quad \text{for} \quad j = 1, 2, \ldots, 40\,.$$

Here β is the angle from the equatorial plane which is defined as the plane of the accretion disk. The geometry is shown in Figure 3. The inclination angle, θ, is defined as the angle between the perpendicular to the plane of the disk and the line of sight to the observer. We truncate the disk above $\beta = 20^\circ$, where the density is taken to be zero, since several of the assumptions entering the building of the disk break down. Since the optical depth along a ray from the center is well below 0.1 at 20°, the results near $\beta = 20^\circ$ should only be influenced at a level of $\sim 10\%$.

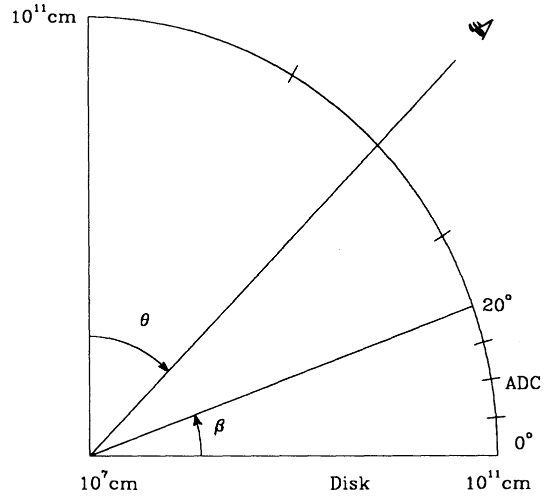

FIG. 3.—Geometry of the accretion disk corona: β is the angle above the disk plane; the inclination angle, θ, is the angle between the perpendicular to the disk plane and the line of sight to the observer.

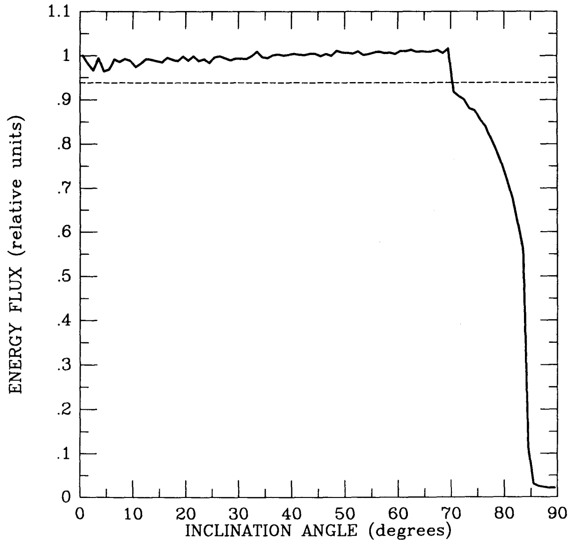

FIG. 4.—Emergent energy as a function of the inclination angle for a power law of $\alpha = 1$ in eq. (1). The dashed horizontal line is the intensity of the undisturbed isotropic emission from the neutron star.

4. RESULTS

4.1. *General Considerations*

The emerging energy as a function of inclination angle for a power law of $\alpha = 1$ (eq. [1]) is given in Figure 4. Since the number of injected particles per unit inclination angle θ varies as sin θ, the fluctuations close to the symmetry axis are large. The sharp break at $\theta = 70^\circ$ results from truncation of the disk corona at this angle (see Fig. 2).

In Figure 5 we present the spectra of the emerging radiation showing photon flux as a function of energy at different inclination angles for three of the four power laws calculated (with photon indices $\alpha = 1, 2, 3$). The photon flux is scaled so that the maximum intensity in the lowest inclination angle bin is 100. The model folded through a typical *EXOSAT* GSPC response matrix is plotted in each figure as a dashed line. The predicted values of the equivalent widths as calculated for the four power laws are depicted as broken lines in Figure 6. The equivalent widths measured from the observations are plotted on Figure 6 as crosses (simultaneous absorption edge detected) and open squares (no absorption edge detected); the best-fit power-law index for each observation is noted next to each point. As can be seen from this figure, the observed values correspond closely to the model predictions: for inclination angles greater than 70°, which in this geometry means that we are looking through the accretion disk corona, and for photon indices less than 3, both line emission and an absorption edge are present; for the steeper indices the absorption edge does not become significant until inclination angles exceed 75° ($\alpha = 3$) and 80° ($\alpha = 4$). Lower inclination angles can show the iron emission feature quite strongly with no indication of an absorption feature. The equivalent width of the Kα feature at a given inclination angle is always lower for the steeper power law. This is because there are relatively fewer photons above the edge in the steeper power law.

4.2. *Individual Sources*

The sources 4U 1735−44, and Sco X-1, with inclination angles less than 30°, show weak iron-line emission with no evidence for an absorption edge. Cen X-3 and SMC X-1, with inclination angles between 30° and 70°, show fairly strong line emission without an absorption edge.

Although Cyg X-2 has an inclination angle of 73°, it has a steep photon index ($\alpha = 2.9$) and thus shows a weak emission line with no perceptible absorption edge. Cyg X-1, which has an ill-determined inclination angle (37°–67°), shows a weak iron line in conjunction with a shallow edge, similar to those from the model for an inclination angle in the range 70°–75° and an incident spectrum of photon index 2.

The sources 4U 1254−64, 4U 1822−37, and Her X-1, with inclination angles greater than 70°, show both line emission and absorption edges, again with the strength of the iron line and depth of the edge dependent on the power-law index.[1]

Our ADC model makes no provision for disruption by the neutron star magnetic field. Disruption of the disk is expected to occur inside the radius where the Keplerian period equals the neutron star spin period (Lamb & Ghosh 1991). Disruption at radii below about 10^9 cm should have little effect on our predictions, and we have restricted ourselves to such systems.

5. DISCUSSION AND CONCLUSIONS

A number of theoretical studies of iron-line emission from LMXBs have appeared over the past few years. These include one-dimensional Monte Carlo treatments in spherical geometry (I85; Koyama 1985, hereafter Koy85; Leahy 1988, hereafter L88; M86; PFR90) and detailed line profile calculations (Kallman & White 1989; Fabian et al. 1989). However, no consistent picture has emerged.

The Monte Carlo techniques applied by I85, Koy85, L88, and M86 to calculate iron-line properties for various discrete geometries were able to obtain spectra that closely resembled some of the observations, but no coherent picture emerged that could reconcile all the data: I85 suggested that pulsars and LMXBs generate iron-line features through different mechanisms, hence produce systematically different spectra (e.g.,

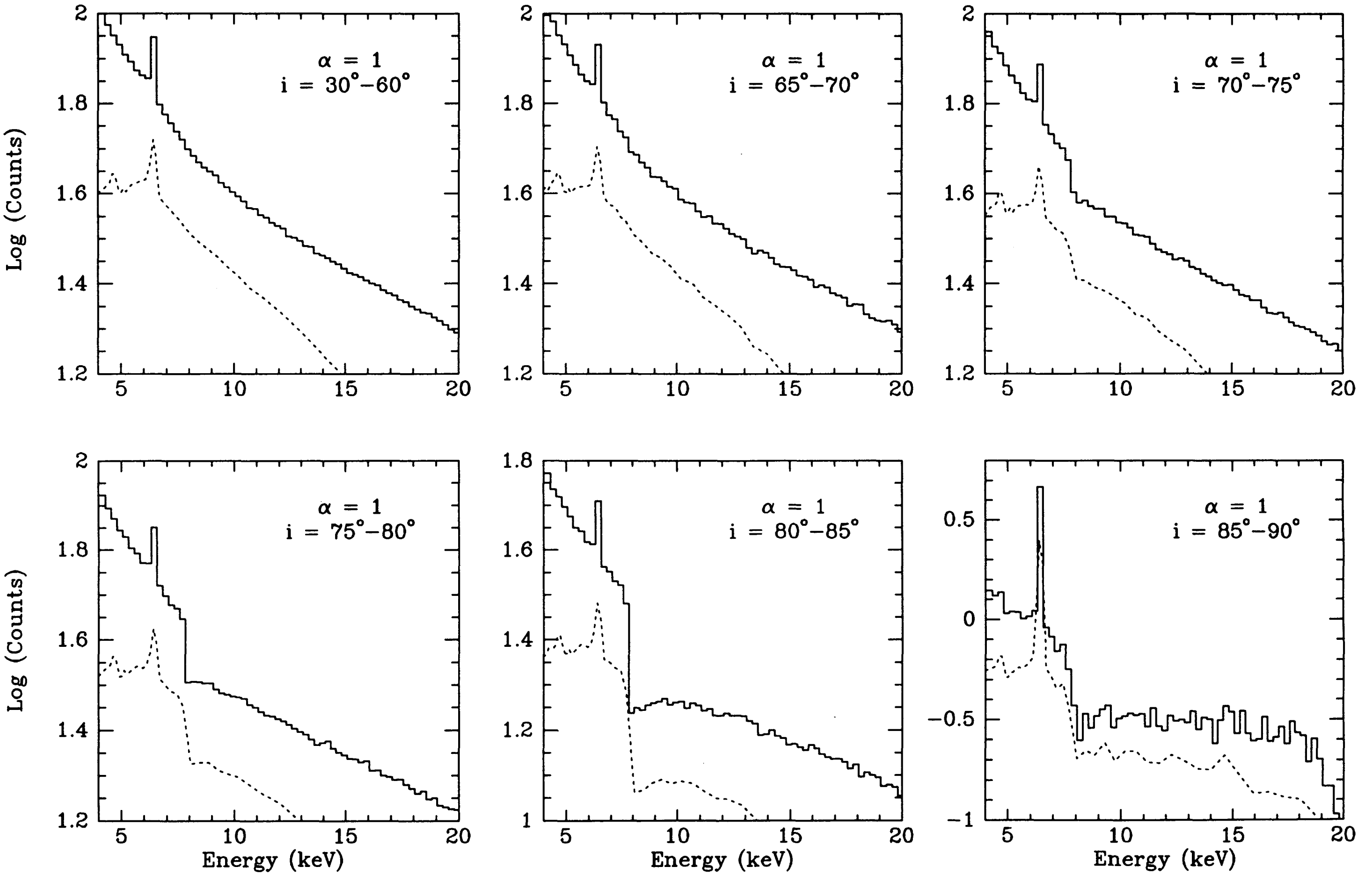

FIG. 5a

FIG. 5.—(*a*) Emerging spectrum for an injected radiation with a power law of $\alpha = 1$ in eq. (1). (*b*) Emerging spectrum for an injected radiation with a power law of $\alpha = 2$ in eq. (1). (*c*) Emerging spectrum for an injected radiation with a power law of $\alpha = 3$ in eq. (1). In each case the photon flux is scaled so that the maximum intensity in the lowest inclination angle bin is 100. The dotted lines represent the model folded through a typical *EXOSAT* GSPC response matrix. Calculated line widths are narrower than the observed iron lines shown in Fig. 1; this discrepancy is partly due to an approximation in the model calculation which collapses the flux from lines in ionization states Fe I–Fe XXV, with energies from 6.4 to 6.7 keV, into flux from Fe XVIII at 6.4 keV. The model also does not include the Keplerian velocities of the ADC; for systems such as Her X-1 this can add up to 0.4 keV line broadening.

---

[1] It has been suggested that the angle of the disk plane to the line of sight of the observer changes as a function of the 36 day cycle, with the changes attributed to disk precession (Corsa & Boynton 1980; Gerend & Boynton 1976). In Table 2 we list two Her X-1 observations, one from the low-on state and one from the high-on state of the 35 day cycle: there is no substantial change in the strength of the iron line (as measured by equivalent width): this suggests that the angle of the disk plane to the line of sight of the observer stays close to 0° throughout the 35 day cycle. A detailed analysis of the *EXOSAT* GSPC data on Her X-1 will be presented elsewhere (Vrtilek et al. 1992).

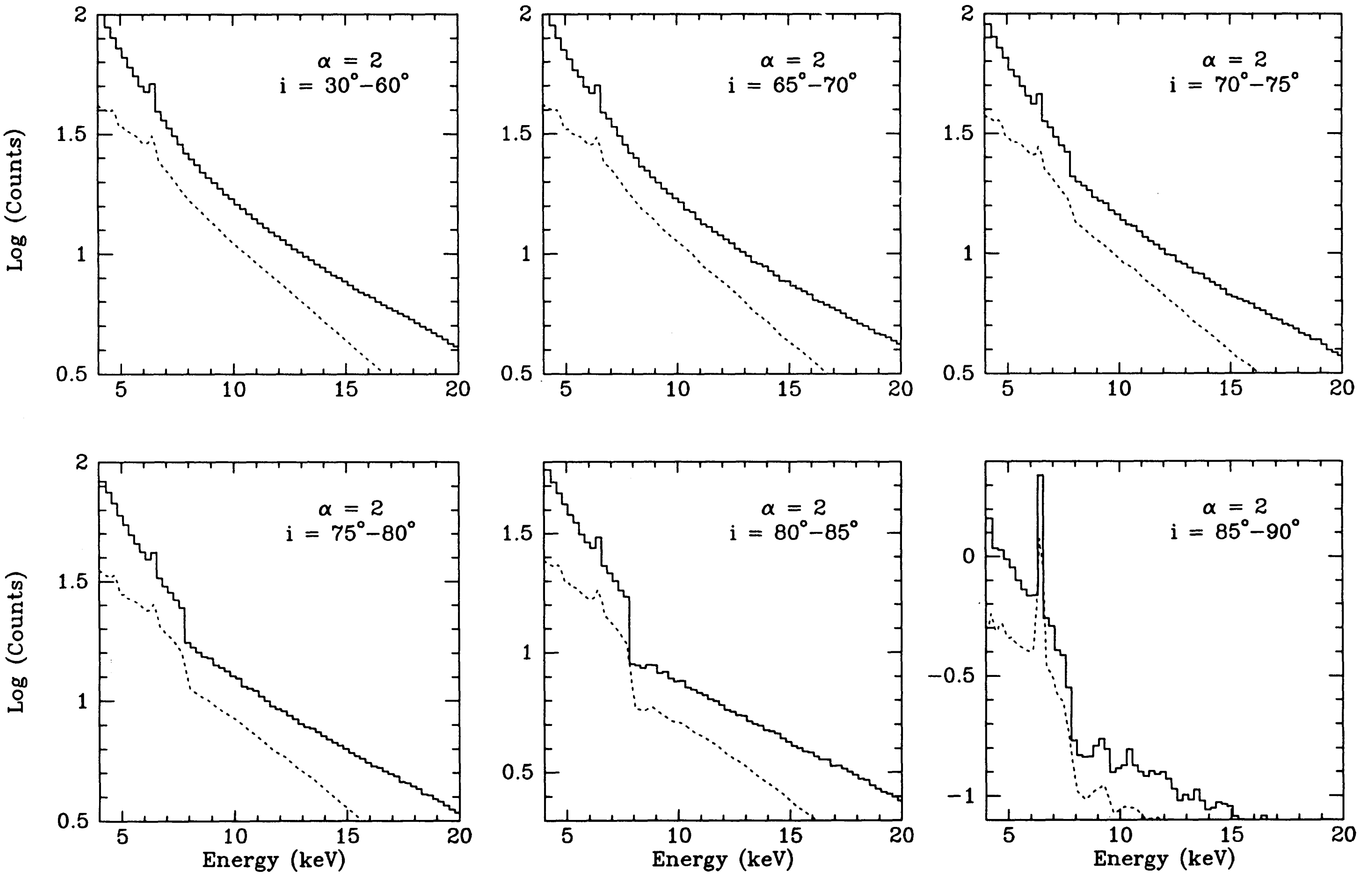
α = 2
i = 30°–60°
α = 2
i = 65°–70°
α = 2
i = 70°–75°
α = 2
i = 75°–80°
α = 2
i = 80°–85°
α = 2
i = 85°–90°
Log (Counts)
Energy (keV)
2
1.5
1
0.5
0
−0.5
−1
5
10
15
20

FIG. 5*b*

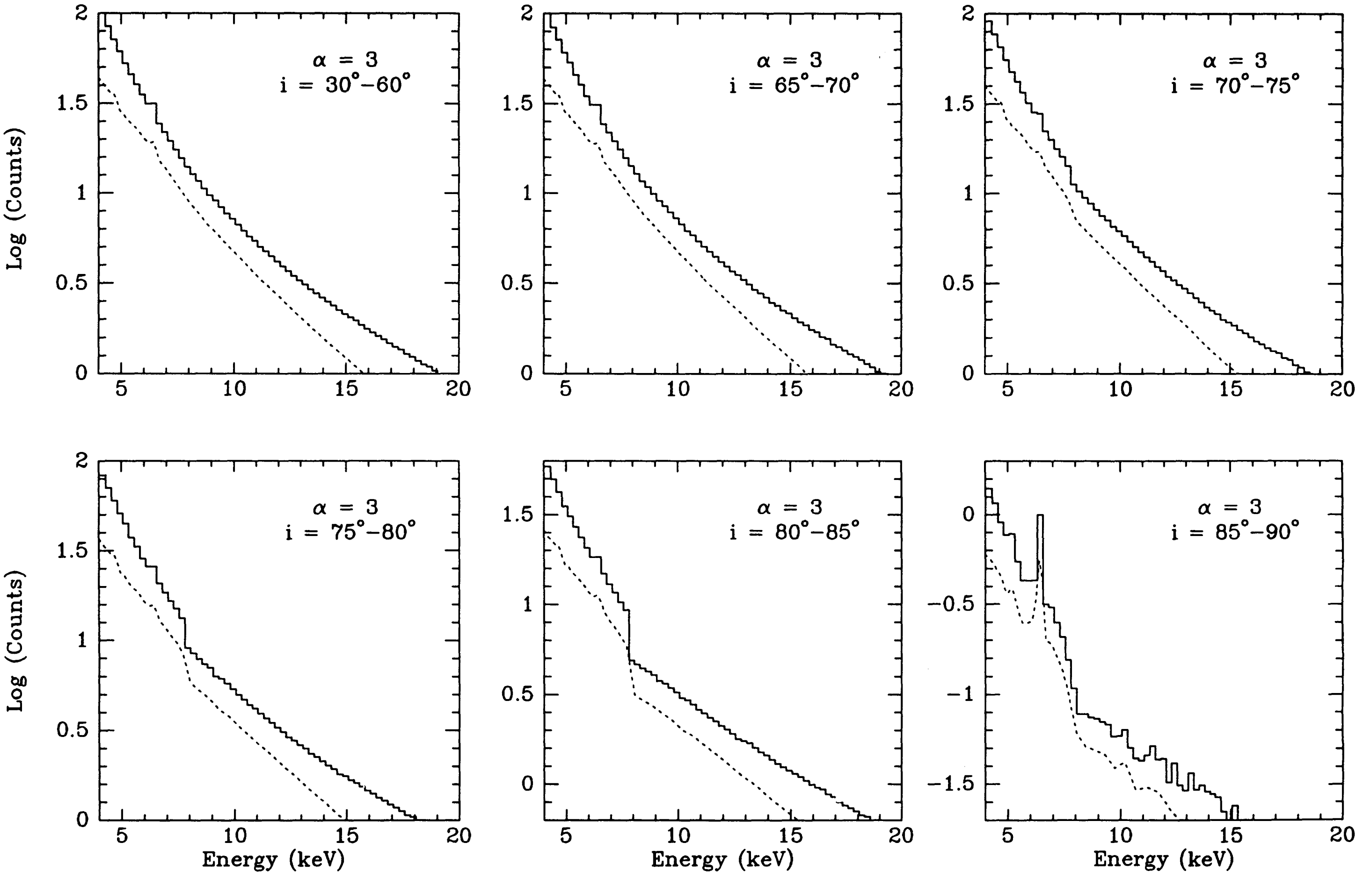
α = 3
i = 30°–60°
α = 3
i = 65°–70°
α = 3
i = 70°–75°
α = 3
i = 75°–80°
α = 3
i = 80°–85°
α = 3
i = 85°–90°
Log (Counts)
Energy (keV)
2
1.5
1
0.5
0
−0.5
−1
−1.5
5
10
15
20

FIG. 5*c*

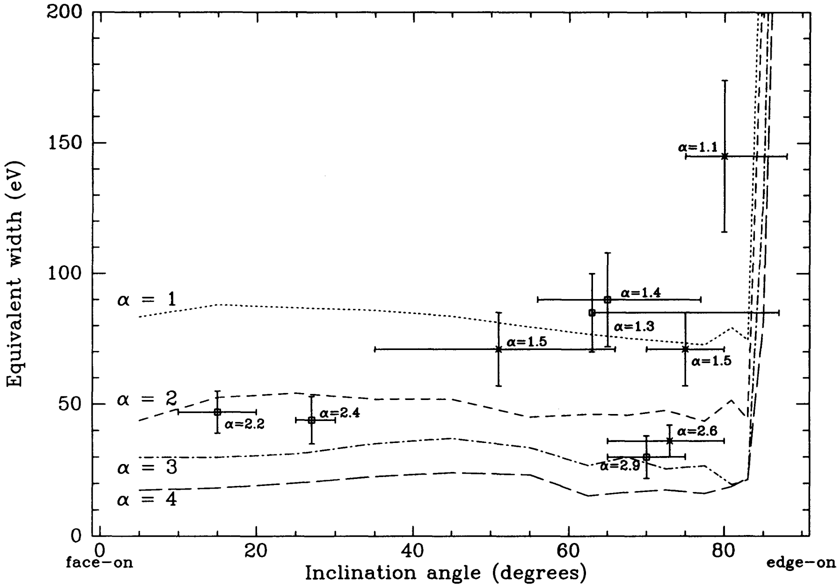

FIG. 6.—Equivalent widths of iron Kα line (Table 2) vs. inclination angles (Table 1). The dotted line represents equivalent width values for a power law with photon index $\alpha = 1$, the short-dashed line for a power law with photon index $\alpha = 2$, the dot-dash line for a power law with photon index $\alpha = 3$, and the long-dashed line for a power law with photon index $\alpha = 4$. The values measured from the observations are shown as crosses (absorption edge detected) and open squares (no absorption edge) with 2 σ error bars. The horizontal error bars indicate uncertainty in the known inclination angle. The best-fit photon index for each source is listed next to the points.

pulsars show absorption edges and LMXBs do not). However, there are counterexamples of both pulsars that do not show an edge (4U 1626−67, SMC X-1, Cen X-3) and LMXBs that do (4U 1608−52, 4U 1254−69, 4U 1822−37). The homogeneous scattering envelope model developed by PFR90 was able to produce the observed strong iron emission only in conjunction with a strong absorption feature, which was not detected in the spectrum of the LMXBs that they were studying.

Kallman & White (1989) used a simplified model for an accretion disk to determine iron-line properties (single-zone models neglecting the dependence of ADC conditions on radial position) with detailed treatment of the line profile. After including the effects of multiple line blending and Comptonization of the line profile, they concluded that Comptonization of the ADC could explain the observed line broadening only if the corona were confined to small radii and the incident X-ray fluxes were very large. Fabian et al. (1989) modeled the iron-line profile of Cyg X-1 assuming that the line originates from a disk surrounding a black hole, and found that the line profile is related to the disk inclination. However, at the resolution of *EXOSAT* their line profiles are indistinguishable from a Gaussian: such calculations must wait for future experiments with very high spectral resolution to allow comparison with data.

Our models differ from the others in that we compute an ADC structure consistent with the X-ray luminosity and accretion rate of the central X-ray source, and we use a two-dimensional Monte Carlo treatment of the radiative transfer within the two-dimensional ADC structure. This leads to a clear prediction for the behavior of the iron equivalent widths with inclination angle and the shape of the incident spectrum, and this prediction agrees with the available data.

We suggest here that the differences attributed by I85 to binary types may in fact be due to inclination angle: in examining the literature, we find that strong line emission and absorption edges are detected preferentially in sources with high inclination angles. The extremely broad lines (FWHM > 1 keV) detected by W86 could be due to failure to include an iron edge; as M86 points out, one can get false line broadening if the continuum model is only slightly wrong. All the lines measured by us were consistent with FWHM < 0.5 keV, the limiting resolution of the instrument. PFR90 were using *EXOSAT* medium-energy data, which has a factor of 2 poorer resolution than the GSPC and is therefore unable to give reliable measurements of iron-line features. It is also possible that the sources PFR90 considered were at low inclination angles: LMXBs in general are noneclipsing systems, which implies either a thick accretion disk or a face-on (i.e., low inclination angle) viewing direction. Of the anomalous pulsars mentioned by I85, 4U 1626−67 has an inclination angle of 18° (van Paradijs 1983), whereas the "normal" pulsar Her X-1, has an inclination angle greater than 70°.

The geometry we have considered is appropriate to primarily disk-fed systems and incorporates a realistic scenario for an accretion disk corona (we have tested the ADC scenario successfully against simultaneous X-ray, UV, and optical observations of Sco X-1 and Cyg X-2; Vrtilek et al. 1990, 1991). Our model is able to reproduce the observed spectral behavior of both pulsars and LMXBs in the 3–20 keV range, predicting the equivalent widths of the emission and absorption features without the introduction of any free parameters to control the physical conditions in the disk corona. The presence or absence of an iron K-edge in the observed spectra is related to the angle between the plane of the disk and the line of sight to the observer and to some extent to the shape of the incident spectrum: the steeper the incident spectrum, the higher the inclination angle at which the absorption edge appears for a given source. The equivalent widths of the iron Kα emission and the depth of the absorption edge are also functions both of the angle of inclination and the shape of the incident source spectrum. The Monte Carlo nature of the model simulations makes direct fitting (in a least-squares sense) to observations difficult but has the potential to determine density and temperature in the line-forming region, a determination not possible with earlier models that treated the continuum- and line-forming regions separately.

Data used in this analysis were taken from the *EXOSAT* archives. The authors would like to thank L. Angelini and N. White for their help in extracting the time-selected data. S. D. V. would like to acknowledge a NASA Long-Term Space Astrophysics Grant (NAGW-2685) and a Marie Curie Fellowship from the AAUW. This work was also partially supported by NASA grant NAGW-528 awarded to J. C. R.

REFERENCES

Barr, P., White, N. E., & Page, C. G. 1985, MNRAS, 216, 65P (BWP85)
Basko, M. M., Sunyaev, R. A., & Titarchuk, L. G. 1974, A&A, 31, 249
Begelman, M. C., McKee, C. F., & Shields, G. A. 1983, ApJ, 271, 70 (BMS83)
Bolton, C. T. 1975, ApJ, 200, 269
Bonnet-Bidaud, J. M., & van der Klis, M. 1981, A&A, 97, 134
Bradt, H. V. D., & McClintock, J. E. 1983, ARA&A, 21, 1
Brinkman, A. C., Mewe, R., Langerwerf, T., Heise, J., Peacock, A., & White, N. 1985, Space Sci. Rev., 40, 201
Chiappetti, L., et al. 1990, ApJ, 361, 596
Clark, G. W., Minato, J. R., & Mi, G. 1988, ApJ, 324, 974
Corbet, R. H. D., Thorstensen, J. R., Charles, P. A., Menzias, J. W., Naylor, T., & Smale, A. P. 1986, MNRAS, 222, 15P
Courvoisier, T. J.-L., Parmar, A. N., Peacock, A., & Pakull, M. 1986, ApJ, 309, 265 (C86)
Cowley, A. P., Crampton, D., & Hutchings, J. B. 1979, ApJ, 231, 847
———. 1982, ApJ, 255, 596
Crampton, D., Cowley, A. P., Hutchings, J. B., & Kaat, C. 1976, ApJ, 207, 907
Crosa, L., & Boynton, P. E. 1980, ApJ, 235, 999
Davis, R., & Hartman, L. 1983, ApJ, 270, 671
Deeter, J. E., Boynton, P. E., & Pravdo, S. H. 1981, ApJ, 247, 1003
Fabian, A. C., Guilbert, P. W., & Ross, R. R. 1982, MNRAS, 199, 1045 (FGR82)
Fabian, A. C., Rees, M. J., Stella, L., & White, N. E. 1989, MNRAS, 238, 729
George, I. M., & Fabian, A. C. 1991, MNRAS, 249, 352
Gerend, D., & Boynton, P. E. 1976, ApJ, 209, 562
Hasinger, G., Langmuir, A., Sztajno, M., Trümper, J., Lewin, W. H. G., & White, N. E. 1986, Nature, 319, 469 (H86)
Hasinger, G., van der Klis, M., Ebisawa, K., Dotani, T., & Mitsuda, K. 1990, A&A, 235, 131
Hellier, C., Mason, K. O., Smale, A. P., & Kilkenny, D. 1990, MNRAS, 244, 39P
Hirano, T., Hayakawa, S., Nagase, F., Masai, K., & Mitsuda, K. 1987, PASJ, 39, 619 (H87)
Inoue, H. 1985, in Japan-U.S. Seminar on Galactic and Extragalactic Compact X-Ray Sources, ed. Y. Tanaka & W. H. G. Lewin (Tokyo: Inst. Space and Astronautical Sci.), 283 (I85)
Kahabka, P. 1987, MPE Rep., No. 204 (K87)
Kahabka, P., Ögelman, H., Pietsch, W., Trümper, J., & Voges, W. 1985, Space Sci. Rev., 40, 355 (K85)
Kallman, T. R., Raymond, J. C., & Vrtilek, S. D. 1991, ApJ, 370, 717
Kallman, T. R., Vrtilek, S. D., & Kahn, S. 1980, ApJ, 345, 498
Kallman, T. R., & White, N. E. 1989, ApJ, 341, 955
Kelly, R. L., Rappaport, S., Clark, G. W., & Petro, L. D. 1983, ApJ, 268, 790
Kitamoto, S., Takahashi, K., Yamashita, K., Tanaka, Y., & Nagase, F. 1990, PASJ, 42, 85 (Kel90)
Koyama, K. 1985, in Japan-U.S. Seminar on Galactic and Extragalactic Compact X-ray Sources, ed. Y. Tanaka & W. H. G. Lewin (Tokyo: Inst. Space and Astronautical Sci.), 153 (Koy85)
Koyama, K., et al. 1984, PASJ, 36, 659
Lamb, F. K., & Ghosh, P. 1991, in Particle Acceleration near Accreting Compact Objects, ed. J. van Paradijs & M. van der Klis (Amsterdam: R. Netherlands Acad. Sci.), in press
Leahy, D. A. 1988, in Physics of Neutron Stars and Black Holes, ed. Y. Tanaka (Tokyo: Universal Academy Press, Inc.) (L88)
Makishima, K. 1986, in Physics of Accretion onto Compact Objects, ed. K. O. Mason, M. G. Watson, & N. E. White (Berlin: Springer-Verlag), 249 (M86)
Mason, K. O. 1986, in Physics of Accretion onto Compact Objects, ed. K. O. Mason, M. K. Watson, & N. E. White (Berlin: Springer-Verlag), 29
McClintock, J. E., London, R. A., Bond, H. E., & Grauer, A. D. 1982, ApJ, 258, 245
Melia, F., Zylstra, G. J., & Fryxell, B. 1991, ApJ, 377, L101
Mertz, A. L., Cowan, R. D., & Magee, N. H., Jr. 1976, Los Alamos Sci. Lab. Rep., No. LA-6220-MS
Morrison, R., & McCammon, D. 1983, ApJ, 270, 119
Motch, C., Pedersen, H., Beuermann, K., Pakull, M., & Courvoisier, T. J.-L. 1987, ApJ, 313, 792
Nagase, F. 1989, PASJ, 41, 1
Nagase, F., Satio, H., Sato, N., Masai, K., & Inoue, H. 1986, PASJ, 38, 547 (N86)
Ostriker, E. C., McKee, C. F., & Klien, R. I. 1990, preprint
Peacock, A., et al. 1982, Space Sci. Rev., 30, 525
Ponman, T. J., Foster, A. J., & Ross, R. R. 1990, MNRAS, 246, 287 (PFR90)
Pozdnyakov, L. A., Sobol, I. M., & Syunyaev, R. A. 1983, Astrophys. Space Phys. Rev., 2, 189 (PSS83)
Smale, A. P., & Corbet, R. H. D. 1991, ApJ, 383, 853
Soker, N., & Raymond, J. C. 1993, in preparation
Vacca, W. D., Sztajno, M., Lewin, W. H. G., Trümper, J., van Paradijs, J., & Smith, A. 1987, A&A, 172, 143
van Paradijs, J. 1983, in Accretion Driven Stellar X-Ray Sources, ed. W. H. G. Lewin & E. P. J. van den Heuvel (Cambridge: Cambridge Univ. Press), 189
Vrtilek, S. D., Kahabka, P., Voges, W., Trümper, J., & Ögelman, H. 1993, in preparation
Vrtilek, S. D., Kahn, S. M., Grindlay, J. E., Helfand, D. J., & Seward, F. D. 1986, ApJ, 307, 698
Vrtilek, S. D., Penninx, W., Raymond, J. C., Verbunt, F., Hertz, P., Wood, K., Lewin, W. H. G., & Mitsuda, K. 1991, ApJ, 376, 278
Vrtilek, S. D., Raymond, J. C., Garcia, M. R., Verbunt, F., Hasinger, G., & Kurster, M. 1990, A&A, 235, 162
Vrtilek, S. D., Swank, J., & Kallman, T. R. 1988, ApJ, 326, 186 (VSK88)
White, N. E., & Holt, S. S. 1982, ApJ, 257, 318 (WH82)
White, N. E., Peacock, A., Hasinger, G., Mason, K. O., Manzo, G., Taylor, B. G., & Branduardi-Raymont, G. 1986, MNRAS, 218, 129 (W86)
White, N. E., Peacock, A., & Taylor, B. G. 1985, ApJ, 296, 475 (WPT85)